Terahertz Superresolution Stratigraphic Characterization of Multilayered Structures Using Sparse Deconvolution

Junliang Dong, Xiaolong Wu, Alexandre Locquet, David S. Citrin

Terahertz Superresolution Stratigraphic Characterization of Multilayered Structures Using Sparse Deconvolution

Junliang Dong, *Student Member, IEEE*, Xiaolong Wu, Alexandre Locquet, and David S. Citrin

***Abstract*—Terahertz sparse deconvolution based on an iterative shrinkage algorithm is presented in this study to characterize multilayered structures. With an upsampling approach, sparse deconvolution with superresolution is developed to overcome the time resolution limited by the sampling period in the measurement and increase the precision of the estimation of echo arrival times. A simple but effective time-domain model for describing the temporal pulse spreading due to the frequency-dependent loss is also designed and introduced into the algorithm, which greatly improves the performance of sparse deconvolution in processing time-varying pulses during the propagation of terahertz waves in materials. Numerical simulations and experimental measurements verify the algorithms and show that sparse deconvolution can be considered as an effective tool for terahertz nondestructive characterization of multilayered structures.**

***Index Terms*—Multilayered structures, nondestructive testing, pulse spreading, sparse deconvolution, superresolution (SR), terahertz (THz) imaging.**

I. Introduction

TERAHERTZ (THz) imaging, as a relatively new and promising nondestructive evaluation (NDE) technique, has attracted considerable interest as a noninvasive, noncontact, and nonionizing method to characterize various nonmetallic materials with multilayered structures [1]–[3]. THz reflective imaging provides information in depth by analyzing the reflected THz signal with an incident approximately single-cycle THz pulse. Due to dielectric discontinuities with depth, reflected temporal THz echoes associated with the Fresnel coefficients between various interfaces are recorded as a function of transverse position in amplitude and time delay. The successful characterization of multilayered structures relies on the precise extraction of echo parameters from the reflected THz signal. For example, characterization of the stratigraphic properties is based on the estimation of arrival times of echoes. In practice, the echoes may partially or totally overlap; therefore, deconvolution is usually required in order to precisely resolve the overlapping echoes and extract the arrival times of superimposed echoes from noisy measurements.

The reflected THz signal is the convolution of the incident THz pulse with the impulse response function, which should ideally consist of a sequence of ideal impulses corresponding to the material structure. Conventional deconvolution aims at retrieving the impulse response function by applying the inverse Fourier transform of the transfer function, which is the ratio of the reflected to the incident THz spectra. However, high-frequency noise will be introduced in this inverse problem, since divisions by small numbers will give rise to large spikes in the high-frequency range, leading to severe ringing in the impulse response function [4]. Therefore, more effort should be made to improve the performance of conventional deconvolution. As a modified version of conventional deconvolution, THz frequency-wavelet domain deconvolution (FWDD) [5] is specifically designed and has been successfully used for locating defects and investigating stratigraphic properties in multilayered structures, such as fiber-reinforced composites [6], polymer coatings [7], art paintings [8], and human skin [5]. The basic idea of FWDD is to enhance the deconvolution process by first employing frequency-domain filtering and then further improving the signal-to-noise ratio (SNR) by wavelet denoising. Baseline subtraction is also needed to cancel the slow fluctuations corresponding to the low-frequency noise due to the deficiency of THz sources in the low THz frequency region. The depth resolution by FWDD is highly dependent on the width of the frequency-domain filter and the SNR. In addition, the time resolution is limited by the discretization precision, corresponding to the data sampling period in the measurement.

The reflected signals from multilayered structures are a class of very special signals comprised of a limited number of echoes, and the corresponding impulse response functions have a sparse representation, which means only a limited number of data points have nonzero values. This feature enables us to exploit the sparse constraint and retrieve the impulse response function by sparse deconvolution. Compared with conventional deconvolution, sparse deconvolution is a pure time-domain method; therefore, there is no introduction of the high- and low-frequency noises mentioned above, and it can be expected to achieve a more

The authors are with the School of Electrical and Computer Engineering, Georgia Institute of Technology, Atlanta, GA 30332 USA, and also with UMI 2958 Georgia Tech-CNRS, Georgia Tech Lorraine, 57070, Metz, France (e-mail: junliang.dong@gatech.edu; xwu@gatech.edu; alexandre@gatech.edu; david.citrin@ece.gatech.edu).

clear representation of the material structures with superresolution (SR) [9]. For 1-D NDE problems, SR techniques seek to recover a high-resolution signal sequence from one or a set of low-resolution acquisition systems. However, sparse deconvolution has not been studied in detail nor has it been extensively used to process THz NDE signals, and to our knowledge, only one attempt has been reported so far. In [10], sparse deconvolution is briefly introduced and used to process THz signals reflected from a human palm.

In this paper, the principle of sparse deconvolution and a computationally efficient iterative shrinkage algorithm for sparse deconvolution are demonstrated to process THz signals reflected from multilayered structures. In order to increase the time resolution, which is limited by the data sampling period, a SR model for sparse deconvolution is developed by an upsampling approach. Based on the assumption that the THz echoes are the time-shifted amplitude-scaled replicas of the THz reference signal, both FWDD and sparse deconvolution are mainly limited to deconvolve reflected THz signals with time-invariant pulses. However, in practice, the temporal pulse spreading caused by frequency-dependent attenuation and dispersion during the propagation of THz waves in materials does occur and, therefore, lowers the performance of deconvolution. In order to solve this problem, a simple but effective time-domain model for describing the pulse spreading is designed and introduced into the algorithm for sparse deconvolution to enhance its ability to deconvolve time-varying echoes. Both numerical simulations and experimental measurements are performed to prove the effectiveness of sparse deconvolution, and the results are also compared with those obtained by FWDD.

II. Principle

A. Sparse Deconvolution With Data Resolution

In the time domain, the THz reflected signal (electric field) $y(t)$ is the convolution of the incident THz pulse $h(t)$ with the impulse-response function $f(t)$, which corresponds to the structure and properties of the sample at a given point of interest

$$y(t) = h(t) \otimes f(t) = \int_{-\infty}^{+\infty} h(\tau) f(t-\tau) d\tau. \tag{1}$$

For reflective THz imaging, the incident THz pulse $h(t)$ can be obtained by first recording the THz signal reflected from a metal plate (THz reference signal) and then multiplying the reference signal by a factor of -1 for phase correction. In practice, we should consider the discrete form of (1) with the sampling period T_s

$$y_n = \sum_{m=0}^{M-1} h_m f_{n-m} + e_n \tag{2}$$

where $y_n = y(nT_s)$, $h_m = h(mT_s)$, and e_n accounts for the noise originating from the measurement system and materials with n and m as the indices of data points, and M as the length of the data points. Let column vectors $\mathbf{y}$, $\mathbf{h}$, $\mathbf{f}$, and $\mathbf{e}$ collect the samples of y_n, h_n, f_n, and e_n, respectively. Then, (2) can be expressed as

$$\mathbf{y} = \mathbf{H}\mathbf{f} + \mathbf{e} \tag{3}$$

where $\mathbf{H}$ is the convolution matrix whose rows are delayed versions of the reversed vector of $\mathbf{h}^{\mathsf{T}}$ or, equivalently, whose columns are delayed versions of $\mathbf{h}$.

The basic idea of sparse deconvolution is to achieve the impulse response function by exploiting the sparse constraint. It aims at approximating the received THz signal $\mathbf{y}$ with $\mathbf{H}\mathbf{f}$, where $\mathbf{f}$ is a sparse sequence, that is, $\mathbf{f}$ has only few nonzero components. In this case, the sparse vector $\mathbf{f}$ can be computed by solving the l_0 regularized optimization problem, which is defined as

$$\min_{\mathbf{f}} \frac{1}{2}\|\mathbf{H}\mathbf{f} - \mathbf{y}\|_2^2 + \lambda \|\mathbf{f}\|_0 \tag{4}$$

where $\|\mathbf{f}\|_0$ is the l_0-norm of $\mathbf{f}$, which is defined to be the number of nonzero entries in $\mathbf{f}$, and λ is the regularization parameter, which controls the tradeoff between the sparsity of $\mathbf{f}$ and the residue norm.

Solving the nonconvex l_0 regularized optimization problem in (4) is known to be nonpolynomial hard, and the global optimum cannot be guaranteed. It has already been shown [11] that this nonconvex optimization problem can be approximated with a convex optimization problem by replacing the l_0 penalty with the l_1 penalty as

$$\min_{\mathbf{f}} \frac{1}{2}\|\mathbf{H}\mathbf{f} - \mathbf{y}\|_2^2 + \lambda \|\mathbf{f}\|_1 \tag{5}$$

where $\|\mathbf{f}\|_1$ is the l_1-norm of $\mathbf{f}$, which is defined as the sum of the absolute values of its components. Since the l_1 norm is convex, a global optimum can be guaranteed.

The iterative shrinkage algorithm, which has been developed recently [12] and is able to address the above optimization problem effectively, is utilized in this paper. Generally speaking, in the iterative shrinkage algorithm, each iteration involves matrix–vector multiplication involving $\mathbf{H}$ and $\mathbf{H}^{\mathsf{T}}$ followed by a shrinkage or soft-thresholding step. Specifically, the general iterative procedure is given by

$$\mathbf{f}_{i+1} = S_{\lambda\tau}\left(\mathbf{f}_i - \tau \mathbf{H}^{\mathsf{T}}(\mathbf{H}\mathbf{f}_i - \mathbf{y})\right) \tag{6}$$

where τ is an appropriate step size, which should obey

$$\tau < \frac{2}{\|\mathbf{H}^{\mathsf{T}}\mathbf{H}\|_2} \tag{7}$$

in order to guarantee convergence, and the shrinkage or soft-thresholding operator $S_{\lambda\tau}$ is defined as

$$S_{\lambda\tau}(f[n]) = \begin{cases} f[n] + \lambda\tau, & f[n] \leqslant -\lambda\tau \\ 0, & |\, f[n]\,| < \lambda\tau \\ f[n] - \lambda\tau, & f[n] \geqslant \lambda\tau. \end{cases} \tag{8}$$

A thorough theoretical analysis in [13] proves the convergence of this iterative shrinkage algorithm guaranteeing that the solution is the global minimizer for convex $\mathbf{f}$. Obviously, the time resolution of the obtained impulse response function $\mathbf{f}$ by sparse deconvoltuion depends upon the time resolution of the reference

signal $\mathbf{h}$, which is itself determined by the discretization precision, corresponding to the data sampling period T_s.

B. Sparse Deconvolution With SR

Compared with conventional deconvolution, one of the advantages of sparse deconvolution is that it can achieve SR. The time resolution of sparse deconvolution can be increased by an upsampling approach. Although the reference signal $h(t)$ is measured at the sampling rate of the data T_s, the original discrete $\mathbf{h}$, which contains M data points, can be upsampled by factor K to form $\mathbf{h}^{sr}$ with time interpolation [14]. In this case, we can consider that the reference signal $h(t)$ is discretized at T_s/K; therefore, the time resolution of $f(t)$ can also be increased by K times accordingly. The discrete convolution model can be written as the sum of K discrete convolutions as

$$y_n = \frac{1}{K}\sum_{k=0}^{K-1}\left(\sum_{m=0}^{M-1} h_m^k f_{n-m}^k\right) + e_n \tag{9}$$

where h^k are K subwavelets with sampling period T_s, such that $h_m^k = h(kT_s/K + mT_s)$, and f^k are the corresponding sparse subsequences with M points. In this model, the discrete convolutions based on the original data and $(K-1)$ times more data points from the time interpolation are summed up and averaged to approximate the received signal $\mathbf{y}$. In this model, we do not perform time interpolation on the received signal $\mathbf{y}$, which is still discretized at T_s with the original data resolution (DR), in order to prevent introducing additional information into $\mathbf{y}$; instead, we apply a sampling and holding approach to deal with $\mathbf{y}$. Then, the matrix form of (9) is

$$\mathbf{y} = \frac{1}{K}\sum_{k=0}^{K-1}\mathbf{H}^k\mathbf{f}^k + \mathbf{e} \tag{10}$$

with $\mathbf{H}^k$ the submatrices obtained by taking every Kth row of $\mathbf{H}^{sr}$, which is the convolution matrix based on $\mathbf{h}^{sr}$. By taking this matrix form into the iterative shrinkage algorithm, the general iterative step should be updated to

$$\mathbf{f}_{i+1}^k = S_{\lambda\tau}\left(\mathbf{f}_i^k - \tau\mathbf{H}^{k\mathsf{T}}\left(\frac{1}{K}\sum_{k=0}^{K-1}\mathbf{H}^k\mathbf{f}_i^k - \mathbf{y}\right)\right) \tag{11}$$

where the step size τ should satisfy

$$\tau < \min_k \frac{2}{\|\mathbf{H}^{k\mathsf{T}}\mathbf{H}^k\|_2} \tag{12}$$

in order to guarantee convergence. By interleaving the obtained K subvectors $\mathbf{f}^k$, the final impulse response function with SR $\mathbf{f}^{sr}$, which contains KM data points, can be achieved.

C. Sparse Deconvolution Considering Pulse Spreading

The performance of sparse deconvolution demonstrated above is mainly limited to the deconvolution of reflective THz signals with time-invariant echoes, which assumes that the THz echoes are time-shifted amplitude-scaled replicas of the THz reference signal. In practice, however, the reflected THz signals can be both sparse and time varying due to the frequency-dependent attenuation and dispersion during the propagation of THz waves in materials. For most of the materials, this frequency-dependent loss has a low-pass filtering effect on the propagating THz waves and results in temporal pulse spreading [15], [16]. For thick multilayered samples in particular, a shape broadening of echoes, which grows as propagation distance increases, can be clearly observed in the received THz signals. This temporal pulse spreading will definitely degrade the accuracy of the sparse deconvolution based on time-invariant echoes.

A simple but effective discrete-time pulse spreading model is designed in the following to solve the problem mentioned above. We assume that the temporal spreading of the propagating THz pulse, caused by traveling a distance slice Δz in an attenuative and/or dispersive medium, can be modeled using a linear time-invariant (LTI) system [17], whose impulse response function is $\rho_{\Delta z}(t)$. At depth Δz, the THz pulse $h_{\Delta z}(t)$ can be expressed as

$$h_{\Delta z}(t) = \rho_{\Delta z}(t) \otimes h_0(t) \tag{13}$$

where $h_0(t)$ is the THz pulse at $\Delta z = 0$, corresponding to the original THz reference signal. Accordingly, a model of the pulse spreading associated with traveling a multiple of this distance, $z_n = N\Delta z$, is obtained by serially connecting the above-mentioned LTI system N times. The impulse response of the serially connected LTI system is modeled as an N-time self-convolution of the impulse response function of the LTI system associated with a material slice of thickness Δz. Therefore, at depth $N\Delta z$, the THz pulse $h_{z_n}(t)$ will be governed by

$$\begin{aligned} h_{z_n}(t) &= \rho_{\Delta z}(t) \otimes \rho_{\Delta z}(t) \otimes \cdots \otimes \rho_{\Delta z}(t) \otimes h_0(t) \\ &= \rho_{\Delta z}^{(N)}(t) \otimes h_0(t) \end{aligned} \tag{14}$$

where $\rho_{\Delta z}^{(N)}(t)$ represents N times self-convolution with the kernel function $\rho_{\Delta z}(t)$.

In the discrete model, the distance slice $\Delta z = cT_s$ corresponds to the data sampling period T_s, with c the propagating speed of THz waves in the material. Because Δz is small, the temporal spreading of the THz pulse between the adjacent distance slices must be relatively small, which implies that the discrete form of the impulse response function $\rho_{\Delta z}[n]$ should be close to a Dirac function delayed one sampling period. This means $\rho_{\Delta z}[n] \approx \delta[n-1]$. In this paper, we model the impulse response function $\rho_{\Delta z}[n]$ for describing the temporal pulse spreading with a simple form:

$$\rho_{\Delta z}[n] = \begin{cases} a, & n = 0 \\ 1-2a, & n = 1 \\ a, & n = 2 \\ 0, & \text{otherwise} \end{cases} \tag{15}$$

where $0 < a \ll 1$ and a determines the severity of the pulse spreading. Note that $a = 0$ yields $\rho_{\Delta z}[n] = \delta[n-1]$, indicating a simple time delay without temporal pulse spreading. In practice, the parameter a can be found by fitting a specific separate echo at a given depth. Let the column vector $\boldsymbol{\rho}$ collect the values of $\rho_{\Delta z}[n]$; then, the matrix $\mathbf{A}$ for describing the pulse spreading throughout the propagating distance can be expressed

as

$$\mathbf{A} = \left[\boldsymbol{\rho}^{(1)}\ \boldsymbol{\rho}^{(2)}\ \boldsymbol{\rho}^{(3)}\ \cdots\ \boldsymbol{\rho}^{(n)}\right] \tag{16}$$

where $\boldsymbol{\rho}^{(n)}$ represents n times self-convolution with the kernel vector $\boldsymbol{\rho}$. Therefore, in order to include the temporal pulse spreading effect, the convolution matrix form in (3) should be modified to

$$\mathbf{y} = \mathbf{HAf} + \mathbf{e} \tag{17}$$

where the matrix $\mathbf{HA}$ models the THz pulse with temporal spreading. Each column of $\mathbf{HA}$ now represents a THz pulse with temporal spreading for a traveling distance equal to $n\Delta z$, where n is also identical to the column number. Compared with the THz pulses in the adjacent columns, both amplitude decrease and shape broadening with respect to the traveling distance can be observed.

Accordingly, in order to deconvolve this kind of time-varying THz signal with the iterative shrinkage algorithm, the general iterative step should be further modified to

$$\mathbf{f}_{i+1} = S_{\lambda\tau}\left(\mathbf{f}_i - \tau(\mathbf{HA})^{\mathsf{T}}(\mathbf{HAf}_i - \mathbf{y})\right) \tag{18}$$

where the step size τ should obey

$$\tau < \frac{2}{\|(\mathbf{HA})^{\mathsf{T}}\mathbf{HA}\|_2} \tag{19}$$

in order to guarantee convergence. It is important to note that (17) indicates that the temporal pulse spreading is considered from the beginning of the received THz signal. However, it is not a common case. For example, in a typical THz reflective imaging experiment, the first columns of $\mathbf{H}$ correspond to the THz pulses propagating in air, which is low loss and involves no pulse spreading. In this case, $\mathbf{A}$ should be divided into two parts by identifying a typical column number n_0, which corresponds to the air/sample interface. To the left of column n_0, $\mathbf{A}$ is composed of an identity matrix $\mathbf{I}$, which is the same as setting $a = 0$, and then, after column n_0, by setting $0 < a \ll 1$, the temporal pulse spreading starts to be involved after the air/sample interface. In the case in which the THz pulse encounters several propagating media, one can build a block diagonal matrix $\mathbf{A}$ composed of the respective media matrices by setting different values of a.

III. Numerical Simulations

Numerical simulations are first performed to verify the iterative shrinkage algorithm for sparse deconvolution with both DR and SR. An actual THz reference signal generated by the experimental system described in Section IV, which contains 4096 data points with a sampling period $T_s = 0.0116$ ps, is recorded and used in the simulations. An ideal and simple impulse response function $f_0[n]$, with the same sampling period and number of data points, is assumed

$$f_0[n] = \begin{cases} 1, & n = 1460 \\ 1, & n = 1550 \\ 0, & \text{otherwise.} \end{cases} \tag{20}$$

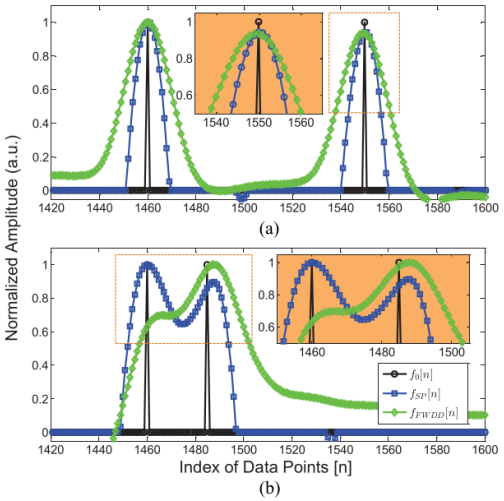

Fig. 1. Comparisons between the assumed (a)$f_0[n]$ and (b)$f_0'[n]$, and the deconvolution results obtained by sparse deconvolution and FWDD, respectively. Insets are the zoom-in images of corresponding boxed peaks.

$f_0[n]$ represents a simple one-layered structure, and the time interval between its two peaks corresponds to the thickness of the structure. $f_0[n]$ is convolved with the reference signal $h[n]$ to simulate the received signal $y_0[n]$. Although $h[n]$ is obtained from an actual noisy measurement, the noise is included in the input signal, which is known *a priori*. Therefore, we consider this simulation as a noise-free case.

Both DR sparse deconvolution and FWDD are employed to solve this inverse problem and recover the impulse response function from $y_0[n]$ with the knowledge of $h[n]$. For sparse deconvolution, the convolution matrix $\mathbf{H}$ is formed by $h[n]$, and the iteration based on (6) is performed 2000 times with the regulation parameter $\lambda = 0.4$ and the step size $\tau = 1/\|\mathbf{H}^{\mathsf{T}}\mathbf{H}\|_2$. For FWDD, a Hanning window function is selected to serve as the frequency-domain filter. Since the depth resolution achieved by FWDD is highly dependent on the cutoff frequency f_c of the frequency-domain filter, we prefer to choose f_c as high as possible; however, with a high value of f_c, a satisfactory SNR of the deconvolved signal may not be guaranteed even after wavelet denosing. In practice, $f_c = 4$ THz is the maximum value we can choose to ensure both a high depth resolution and a satisfactory SNR. Baseline subtraction is performed on the deconvolved signal by FWDD. Other parameters in FWDD can be found in [8].

The simulation results are shown in Fig. 1(a). It can be seen that the deconvolution results, $f_{\mathrm{SP}}[n]$ and $f_{\mathrm{FWDD}}[n]$, which are obtained from DR sparse deconvolution and FWDD, respectively, successfully recover the assumed impulse response function, as the locations of the pulses in $f_{\mathrm{SP}}[n]$ and $f_{\mathrm{FWDD}}[n]$ exactly match the peaks in $f_0[n]$. The width of the pulses obtained by sparse deconvolution is narrower than that obtained by FWDD, which indicates the potential that the minimal time interval resolved with DR sparse deconvolution can be smaller than that

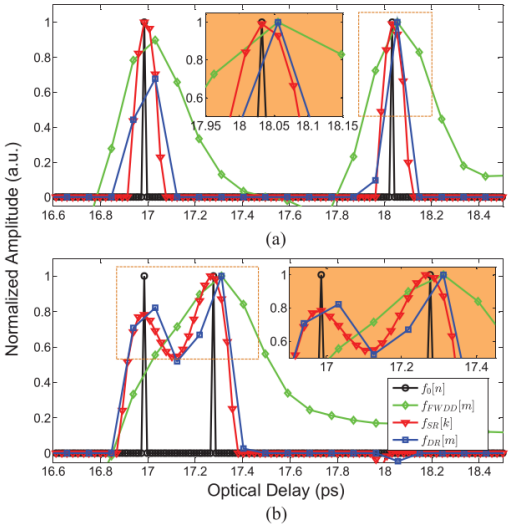

Fig. 2. Comparisons between the assumed (a)$f_0[n]$ and (b)$f_0'[n]$, and the deconvolution results obtained by DR sparse deconvolution and SR sparse deconvolution with $K = 4$ and FWDD, respectively. Insets are the zoom-in images of corresponding boxed peaks.

with FWDD. The minimal time interval which DR sparse deconvolution is able to resolve can be identified by varying the distance between the two peaks in $f_0[n]$. We determine that the impulse response function with minimal resolvable time interval $f_0'[n]$ is as follows:

$$f_0'[n] = \begin{cases} 1, & n = 1460 \\ 1, & n = 1485 \\ 0, & \text{otherwise} \end{cases} \tag{21}$$

in which the time interval between two peaks equals $25T_s$. The deconvolution results are shown in Fig. 1(b). We observe that two peaks can be identified based on the results from DR sparse deconvolution, while only one peak can be located based on the results from FWDD. It is important to note that, in practice, for both FWDD and sparse deconvolution, the minimal thickness resolution, corresponding to the depth resolution, is dependent on the coherence length, the sampling frequency, and the SNR.

Next, SR sparse deconvolution is utilized to recover $f_0[n]$ and $f_0'[n]$ based on signals with lower time resolution. Both $f_0[n]$ and $f_0'[n]$ are convolved with the reference signal $h[n]$, and after convolution, the signals are undersampled by a factor 8 to simulate the received signals $y_0[m]$ and $y_0'[m]$, which contain only 512 data points corresponding to a data sampling period $T_s' = 8T_s$. In this case, we consider the time resolution of $y_0[m]$ and $y_0'[m]$ as the DR. Both DR sparse deconvolution and SR sparse deconvolution are performed based on $y_0[m]$, $y_0'[m]$, and $h'[m]$, which is accordingly the undersampled version of $h[n]$ by a factor 8. In this simulation, the maximum undersampling factor is limited by the Nyquist sampling frequency to ensure that all the information in the received signal is sampled.

The deconvolution results are shown in Fig. 2 for both cases. The DR deconvolution results, $f_{\text{DR}}[m]$ and $f_{\text{FWDD}}[m]$, which

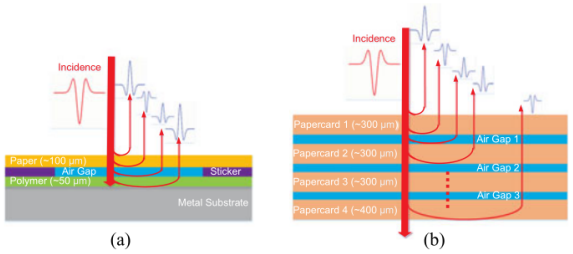

Fig. 3. Two samples with multilayered structures. (a) Sample A: a three-layered structure, which is composed of one copy paper, air gap, and one polymer coating. (b) Sample B: a seven-layered structure, which is composed of four different papercards with air gaps between them.

are obtained from DR sparse deconvolution and FWDD, respectively, cannot recover the assumed impulse response functions with enough accuracy, as the locations of the peaks in $f_{\text{DR}}[m]$ and $f_{\text{FWDD}}[m]$ do not exactly match the peaks in $f_0[n]$. In order to increase the accuracy and time resolution, SR sparse deconvolution based on (11) is employed, and the SR achieved is determined by the upsampling factor K. In our simulations, with $K = 4$, the SR deconvolution results $f_{\text{SR}}[k]$ successfully recover the assumed impulse response function $f_0[n]$, as the locations of the peaks in $f_{\text{SR}}[k]$ exactly coincide with the assumed peaks in $f_0[n]$. It is noted that the accuracy of $f_{\text{SR}}[k]$ is also affected by the start point in the undersampling period; in this simulation, with only four times upsampling, we can achieve an accurate recovery. The results thus show that SR sparse deconvolution can overcome the limitation of DR and recover the impulse response function with SR.

IV. Samples and Experiment

Two samples with multilayered structures are fabricated to verify and evaluate the performance of sparse deconvolution experimentally. The first sample (Sample A), shown in Fig. 3(a), is a three-layered structure made by sticking one layer of paper on a polymer-coated steel plate, with an air gap intentionally introduced between the paper (thickness ~ 100 μm) and the polymer coating (thickness ~ 50 μm). The second sample (Sample B), shown in Fig. 3(b), is a seven-layered structure obtained by stacking four different papercards. The thicknesses of the first three papers are about 300 μm, and the thickness of the fourth papercard is about 400 μm. Since the papercards are not compressed tightly, air gaps with different thicknesses are also introduced between the papercards.

A standard THz time-domain spectroscopy system (Teraview TPS Spectra 3000) is employed in this study to perform THz reflective imaging at almost normal incidence on these two samples. Before studying the samples, the THz reference signal, shown in Fig. 4, is recorded by setting a metal plate at the sample position. The data sampling period in the measurement is set to $T_s = 0.093$ ps. Each recorded reflected temporal THz waveform contains 512 data points, and the signal is averaged over ten shots. DR sparse deconvolution is applied to reconstruct the sample structures based on the received signals. For the three-layered sample, SR sparse deconvolution is

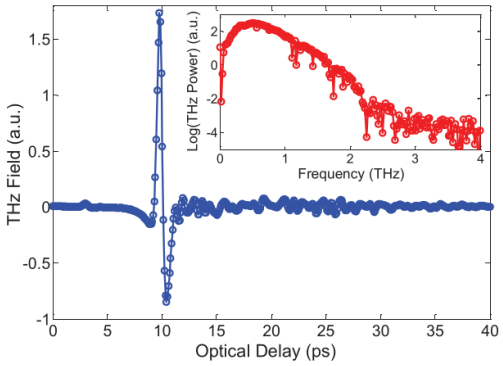

Fig. 4. THz reference signal used in the deconvolution of experimental THz received signals, which contains 512 data points with sampling period $T_s = 0.093$ ps. The inset is the frequency spectrum of this reference signal.

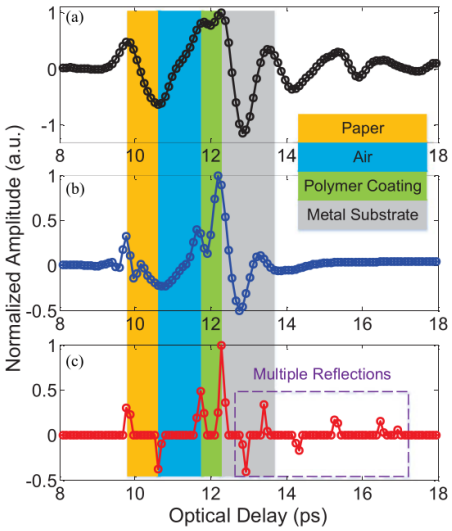

Fig. 5. Raw and deconvolved signals for Sample A. (a) Received THz signal from Sample A. (b) Deconvolved signal with FWDD. (c) Deconvolved signal with DR sparse deconvolution.

further applied to increase the time resolution of the arrival times of echoes. Since both the THz loss and the propagating distance are relatively large in the seven-layered sample, sparse deconvolution including temporal pulse spreading described in Section II-C is implemented to increase the accuracy of the reconstruction.

V. Results and Discussion

A typical received THz signal reflected from Sample A is shown in Fig. 5(a). Since the thickness of each layer is optically thin in the THz regime, this received THz signal is the superposition of several echoes, corresponding to the internal interfaces in the sample. Both DR sparse deconvolution and FWDD are implemented to deconvolve the received signal, and the results are compared. It is important to note that, in this section, we

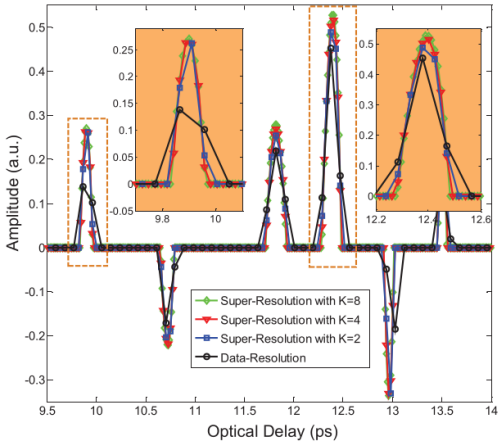

Fig. 6. Comparison between the DR deconvolved signal and the SR deconvolved signals with the upsampling factor $K = 2, 4$, and 8. Two insets are the zoom-in version of the first and fourth peaks.

consider the THz reference signal (shown in Fig. 4) as the input and the received THz signal as the output; therefore, the actual impulse response function associated with the reflection coefficients should be obtained by multiplying the deconvolved signal by a factor of "-1" for phase correction.

For DR sparse deconvolution, the convolution matrix $\mathbf{H}$ is formed by the experimentally obtained reference THz signal, which contains 512 data points, and the iteration based on (6) is performed 2000 times with the regulation parameter $\lambda = 0.2$ and the step size $\tau = 0.1/\|\mathbf{H}^{\mathrm{T}}\mathbf{H}\|_2$. For FWDD, we utilize the same parameters as the ones we used in the simulations, as $f_c = 4$ THz is the maximum value we can set to ensure the deconvolved signal with both a high depth resolution and a satisfactory SNR. The deconvolved signals with both methods are shown in Fig. 5(b) and (c). Both of the deconvolved signals can recover the main features of the sample structure. However, by comparison, we can find out that the deconvolved signal from DR sparse deconvolution, which contains sharp peaks and no slow fluctuations, is capable of providing a more clear representation of the various interfaces in the sample than that from FWDD. Furthermore, DR sparse deconvolution is also more effective in resolving small echoes due to the multiple reflections in the samples. The thicknesses of the paper, the air gap, and the polymer coating can be calculated based on the measurement of the optical delay between relevant peaks and the knowledge of the refractive indexes. As mentioned before, the time resolution of the locations of echoes is limited by the sampling period T_s in the experiment.

SR sparse deconvolution is further implemented on the received signal from Sample A to increase the time resolution for more accurate thickness calculation. The SR deconvolved signals with an upsampling factor $K = 2, 4$, and 8 are shown in Fig. 6 and are compared with the DR deconvolved signal. As K increases, the accuracy in locating the positions of echoes increases, which leads to a more accurate thickness calculation. It is also noticed that the upsampling factor K does not need to be too large, as the SR deconvolved signals with $K = 4$ and

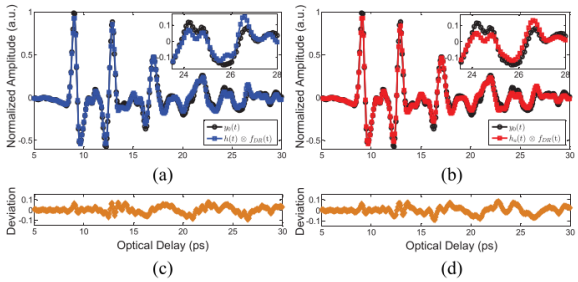

Fig. 7. Comparison between the received signal and the reconvolution signal. (a) Comparison between the reconvolution without considering the pulse spreading effect and the actual received signal, and the inset is the zoom-in of the last echo. (b) Comparison between the reconvolution considering the pulse spreading effect and the actual received signal, and the inset is the zoom-in of the last echo. (c) Deviation between $h(t) \otimes f_{\mathrm{DR}}(t)$ and $y_0(t)$ in (a). (d) Deviation between $h_a(t) \otimes f_{\mathrm{DR}}(t)$ and $y_0(t)$ in (b).

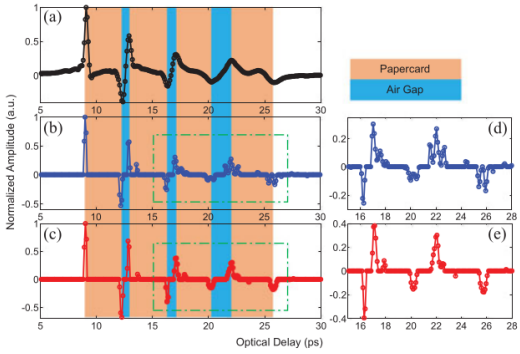

Fig. 8. Comparison between the deconvolved signals with and without considering the temporal pulse spreading effect. (a) Deconvolved signal with FWDD. (b) Deconvolved signal with sparse deconvolution without considering the pulse spreading. (c) Deconvolved signal with sparse deconvolution including pulse spreading. (d) Zoom-in of the last three interfaces in (b). (e) Zoom-in of the last three interfaces in (c).

8 provide almost the same locations of echoes. The time resolution achieved here by SR sparse deconvolution is actually limited by the SNR in the received THz signal [18].

Based on the raw and deconvolved signals from Sample A, no temporal pulse spreading is clearly observed, since the thickness of sample is relatively small. Sample B, however, is thicker and displays pulse spreading when the THz pulse propagates through. The typical received signal $y_0(t)$ reflected from Sample B is shown in Fig. 7 in black. Since the thicknesses of the papercards are large enough, the reflected THz pulses corresponding to the various interfaces between papercards can be clearly identified. However, each pulse indicating the location of the interface is still the superposition of the echoes bouncing back from the front and back interfaces of the air gaps. As the propagating distance increases, a shape broadening can be observed in the THz echoes, which corresponds to the temporal pulse spreading due to the attenuation and dispersion in the papercards. The deconvolved signals with FWDD and DR sparse deconvolution without pulse spreading are shown in Fig. 8(a) and (b). Compared with FWDD, sparse deconvolution is more effective in resolving small echoes due to multiple reflections, as smaller amplitudes following the main pulses corresponding to the air/papercard interfaces can be clearly observed, shown in Fig. 8(b). For the deconvolved signal with FWDD, it is obvious that this pulse spreading can also lower the performance of FWDD, as the peaks indicating the locations of interfaces become wider as the propagating distance increases. For the deconvolved signal with DR sparse deconvolution without pulse spreading, the peaks corresponding to the echoes bouncing back from the first and second papercards are quite sharp; however, additional small peaks appear at the last three interfaces, which will definitely obscure the exact locations of the interfaces. The origin of these additional peaks is the temporal pulse spreading. Without including this pulse spreading effect in the algorithm, the input signal is considered as invariant, which is the narrow THz reference signal, and thus, a wider THz echo in the received signal will be treated as a combination of several narrow pulses.

In order to obtain the deconvolved signal with definite and clear locations of interfaces, it is necessary to utilize the sparse deconvolution including pulse spreading to deal with the received signal reflected from Sample B. The most important step in this algorithm is the formation of the matrix $\mathbf{A}$. By peak detection, the location of the first air/papercard interface can be identified. This location is considered as the typical column number n_0. Above n_0, $\mathbf{A}$ is filled with an identity matrix, and after n_0, $\mathbf{A}$ is formed based on (16). The key parameter a is determined by multiple trials. In our case, the criterion for the fitness of a is based on the last received THz pulse corresponding to the interface between the back of the last papercard and the air, which should satisfy the following conditions: 1) the deconvolved signal achieved $f_{\mathrm{DR}}(t)$ should provide one sharp and clear pulse corresponding to the location of the last interface; and 2) $f_{\mathrm{DR}}(t)$ is convolved with the input signal including pulse spreading $h_a(t)$, and there should be a good fit between the convolution result $h_a(t) \otimes f_{\mathrm{DR}}(t)$ and the received THz signal $y_0(t)$, especially for the last THz pulse. The optimal value we determine in the algorithm is $a = 0.035$, and the corresponding deconvolved signal is shown in Fig. 8(c). We observe that, by considering the pulse spreading effect, the spurious peaks, which appear in Fig. 8(b), are eliminated, and all the interfaces are clearly located by sharp pulses. Furthermore, the accuracy of the deconvolved signals is confirmed by the reconvolution and the comparison with the actual received THz signal $y_0(t)$, shown in Fig. 7. By carefully checking the deviation between the reconvolution and the actual received signal, shown in Fig. 7(c) and (d), the deconvolved signal with pulse spreading is more accurate, since smaller ripples in the fluctuations of the deviation can be observed in the region of late-coming echoes. The zoom-in insets of the last THz echoes in Fig. 7(a) and (b) further prove the validity of this algorithm.

VI. Conclusion

In this study, sparse deconvolution based on an iterative shrinkage algorithm has been demonstrated for THz characterization of multilayered structures. Compared with conventional deconvolution, such as FWDD, in which high- and low-frequency noises are inevitably introduced, sparse deconvolution is a pure time-domain technique, which can provide a more clear representation of the impulse response function with

sharp pulses. Since the time resolution of conventional deconvolution is limited by the discretization precision, an SR version of sparse deconvolution is further developed by an upsampling approach based on time interpolation, which increases the capability of sparse deconvolution for precise estimation of the arrival times of THz echoes. In addition, the temporal pulse spreading due to the frequency-dependent loss during the THz propagation is also considered in the sparse deconvolution. A simple but effective time-domain model for describing the temporal pulse spreading effect is designed and introduced into the iterative shrinkage algorithm. This model requires little prior knowledge of the properties and structure of the materials and can greatly improve the performance of sparse deconvolution in processing time-varying THz pulses. The algorithms for sparse deconvolution are all verified with numerical simulations and experimental measurements, which demonstrate that sparse deconvolution is an ideal and effective tool for THz nondestructive characterization of multilayered structures.

REFERENCES

[1] J. Dong, B. Kim, A. Locquet, P. McKeon, N. Declercq, and D. S. Citrin, "Nondestructive evaluation of forced delamination in glass fiber-reinforced composites by terahertz and ultrasonic waves," *Composites B, Eng.*, vol. 79, pp. 667–675, 2015.

[2] S. Krimi, J. Klier, J. Jonuscheit, G. Von Freymann, R. Urbansky, and R. Beigang, "Highly accurate thickness measurement of multi-layered automotive paints using terahertz technology," *Appl. Phys. Lett.*, vol. 109, 2016, Art. no. 021105.

[3] Y.-C. Shen and P. F. Taday, "Development and application of terahertz pulsed imaging for nondestructive inspection of pharmaceutical tablet," *IEEE J. Sel. Topics Quantum Electron.*, vol. 14, no. 2, pp. 407–415, Mar./Apr. 2008.

[4] G. C. Walker *et al.*, "Terahertz deconvolution," *Opt. Exp.*, vol. 20, no. 25, pp. 27230–27241, 2012.

[5] Y. Chen, S. Huang, and E. Pickwell-MacPherson, "Frequency-wavelet domain deconvolution for terahertz reflection imaging and spectroscopy," *Opt. Exp.*, vol. 18, no. 2, pp. 1177–1190, 2010.

[6] N. Palka, R. Panowicz, M. Chalimoniuk, and R. Beigang, "Non-destructive evaluation of puncture region in polyethylene composite by terahertz and X-ray radiation," *Composites B, Eng.*, vol. 92, pp. 315–325, 2016.

[7] J. Dong, A. Locquet, and D. S. Citrin, "Terahertz quantitative nondestructive evaluation of failure modes in polymer-coated steel," *IEEE J. Sel. Topics Quantum Electron.*, vol. 23, no. 4, pp. 1–7, Jul./Aug. 2017.

[8] J. Dong *et al.*, "Terahertz frequency-wavelet domain deconvolution for stratigraphic and subsurface investigation of art painting," *Opt. Exp.*, vol. 24, no. 23, pp. 26972–26985, 2016.

[9] G.-M. Zhang, C.-Z. Zhang, and D. M. Harvey, "Sparse signal representation and its applications in ultrasonic NDE," *Ultrasonics*, vol. 52, no. 3, pp. 351–363, 2012.

[10] E. P. J. Parrott, S. M. Y. Sy, T. Blu, V. P. Wallace, and E. Pickwell-MacPherson, "Terahertz pulsed imaging in vivo: measurements and processing methods," *J. Biomed. Opt.*, vol. 16, no. 10, pp. 106010–106018, 2011.

[11] T. Blumensath and M. E. Davies, "Iterative thresholding for sparse approximations," *J. Fourier Anal. Appl.*, vol. 14, no. 5, pp. 629–654, 2008.

[12] M. Elad, B. Matalon, J. Shtok, and M. Zibulevsky, "A wide-angle view at iterated shrinkage algorithms," *Proc. SPIE*, vol. 6701, 2007, Art. no. 670102.

[13] I. Daubechies, M. Defrise, and C. De Mol, "An iterative thresholding algorithm for linear inverse problems with a sparsity constraint," *Commun. Pure Appl. Math.*, vol. 57, no. 11, pp. 1413–1457, 2004.

[14] E. Carcreff, S. Bourguignon, J. Idier, and L. Simon, "High-resolution deconvolution applied to non destructive testing," in *Proc. Acoust. Conf.*, Nantes, France, 2012, pp. 2976–2980.

[15] A. Redo-Sanchez *et al.*, "Terahertz time-gated spectral imaging for content extraction through layered structures," *Nature Commun.*, vol. 7, 2016, Art. no. 12665.

[16] S. Zhou *et al.*, "Terahertz signal classification based on geometric algebra," *IEEE Trans. THz Sci. Technol.*, vol. 6, no. 6, pp. 793–802, Nov. 2016.

[17] T. Olofsson and T. Stepinski, "Minimum entropy deconvolution of pulse-echo signals acquired from attenuative layered media," *J. Acoust. Soc. Amer.*, vol. 109, no. 6, pp. 2831–2839, 2001.

[18] E. J. Candès and C. Fernandez-Granda, "Super-resolution from noisy data," *J. Fourier Anal. Appl.*, vol. 19, no. 6, pp. 1229–1254, 2013.